



**Molecular dynamics simulation study of linear, bottlebrush,
and star-like amphiphilic block polymer assembly in
solution**

Journal:	<i>Soft Matter</i>
Manuscript ID	SM-ART-02-2019-000375.R1
Article Type:	Paper
Date Submitted by the Author:	04-Apr-2019
Complete List of Authors:	Wessels, Michiel; University of Delaware, Chemical and Biomolecular Engineering Jayaraman, Arthi; University of Delaware, Chemical and Biomolecular Engineering

(submitted to *Soft Matter*)

Molecular dynamics simulation study of linear, bottlebrush, and star-like amphiphilic block polymer assembly in solution

Michiel G. Wessels¹, and Arthi Jayaraman^{1,2,}*

1. 150 Academy Street, Colburn Laboratory, Department of Chemical and Biomolecular Engineering,

University of Delaware, Newark, DE 19716

2. Department of Materials Science and Engineering, University of Delaware, Newark, DE 19716

***Corresponding author E-mail:** arthij@udel.edu

Abstract

In this study we investigate the effect of varying branched polymer architectures on the assembly of amphiphilic block polymers in solution using coarse-grained molecular dynamics simulations. We quantify assembly structure (*e.g.*, aggregation number, assembly morphology, and micelle core size) and thermodynamics (*e.g.*, unimer to micelle transition conditions) as a function of increasing solvophobicity of the solvophobic block in the copolymer for three broad categories of polymer architectures: linear, ‘bottlebrush’ (with many short side chains on a long backbone), and ‘star-like’ (with few long side chains on a short backbone). Keeping the total number of coarse-grained beads in each polymer (or polymer molecular weight) constant, as we go from either linear or ‘star-like’ to bottlebrush polymer architectures, the micelle aggregation number and micelle core size decrease, and the solvophobicity required for assembly (*i.e.* transition solvophobicity) increases. This trend is linked to the topological/steric hinderance for making solvophobic bead contacts between neighboring polymers for the ‘bottlebrush’ polymer architecture compared to the linear or ‘star-like’ architectures. We are able to identify some universal trends in assembly by plotting the assembly structure and thermodynamics data as a function of branching parameter defined as the ratio of the branched chain to the linear chain radius of gyration in the unimer state, and the relative lengths of the backbone versus side chain. The results in this paper guide how one could manipulate the amphiphilic block polymer assembly structure and thermodynamics by choosing appropriate polymer architecture, block sequence, and composition.

1. Introduction

Nanostructured assemblies of amphiphilic block polymers in solution are designed for use in a variety of applications that include removal of pollutants from the environment, drug delivery, nanoreactors, and bio-imaging, as described in many review articles.¹⁻¹³ Block polymer (BP) self-assembly into micelles is driven by the competing interactions between the two or more polymer block types and the solvent or solvent mixture.^{8, 14-16} The assembled state characteristics (*e.g.* micelle size, morphology, and stability in different solvent conditions) are controlled by the polymer block sequence (*e.g.* AB, ABA, or BAB), molecular weight, amphiphilic composition (*e.g.* solvophobic or solvophilic composition), polymer concentration (*e.g.* dilute versus semi-dilute), and the polymer architecture (*e.g.* linear, cyclic, star, dendrimer, or bottlebrush).^{1-10, 12, 16-21}

Linear BP self-assembly in solution has been investigated extensively over past few decades.^{3-13, 15-20} With recent advances in polymer synthesis schemes, self-assembly of complex non-linear polymer architectures, such as bottlebrush BPs, have begun to receive more attention (see review articles^{11, 13}). The bottlebrush architecture is comprised of a linear backbone with densely grafted linear/non-linear side chains. This complex architecture allows for unique physicochemical properties such as a tunable chain size and stiffness simply by changing the grafting density, length, and architecture of the side chains.²²⁻²⁴ Controlled synthesis where the bottlebrush backbone and side chain lengths are varied independently, achieving different BP sequences, has also been demonstrated.^{11, 25, 26} The self-assembly of bottlebrush BPs has been studied in bulk/near interfaces, in melt conditions,²⁷⁻³⁵ and dilute concentrations using experimental³⁶⁻⁴⁵ and computational⁴⁶⁻⁵⁵ techniques. Micellization of bottlebrush diblock polymers (di-BPs) has many favorable features over micelles formed from linear di-BPs. For example, bottlebrush BPs exhibit a smaller critical micelle concentration than lower molecular weight, linear BPs of similar chemistry.^{11, 36, 45} The size distribution of micelles formed by bottlebrush BPs is easily controlled by modifying the ratio of solvophobic to solvophilic side chain length.²⁹ Lastly, the side chain chains provide functionalizable end group chemistries such as groups with high contrast for imaging or cross-linkable groups that can stabilize

the micelle after assembly.^{11, 36, 40}

Star polymer architectures also influence the self-assembly of BPs in solution and offer additional methods to target specific micelle characteristics. Experimental studies⁸ compare the self-assembly of star polymer architectures in solution (with different combinations of one to two solvophilic and/or solvophobic arms) to the assembly of linear BPs of similar chemistry and molecular weight. The comparison indicates that star BPs have lower aggregation numbers, smaller micelle sizes and higher critical micelle concentrations (CMC) than their linear equivalents.⁸ A theoretical study has also shown that varying the number of arms for the star BPs, at the same or different molecular weight, tunes the core-corona interface and in some cases, destabilizes spherical assembled morphologies with an increasing number of solvophobic polymers arms due to the entropic penalty of stretching a larger number of chains in the micelle core.⁵⁶

In this paper, we use coarse-grained molecular dynamics (MD) simulations to systematically investigate the effect of BP branching on the micelle thermodynamics (unimer to micelle transition, favorable energetic contacts, and conformational entropy) and assembly structure (micelle aggregation number, size, and morphology) for increasing solvophobicity of the solvophobic B block in the amphiphilic polymers with varying polymer sequence (AB, ABA, and BAB), and composition (75% solvophobic B block to 25% solvophobic B block). We vary BP branching by decreasing the backbone length while simultaneously increasing the side chain length to maintain the same total number of coarse-grained polymer beads in all BPs. We find that there is a non-monotonic behavior in the assembly thermodynamics (*i.e.*, the solvophobicity required to form micelles), the aggregation number, and the micelle size as we go from linear to bottlebrush (with many short side chains on a long backbone) to ‘star-like’ (with few long side chains on a short backbone) BP architectures. We establish some universal trends by describing all of the above results as a function of branching parameter⁵⁷ and relative lengths of backbone versus side chain length.

The rest of our paper is organized as follows. In section 2, we describe the polymer model used in

the MD simulations, the MD simulation procedure and analyses, and the parameter space explored in this study. In section 3, we present and discuss our results for the different polymer architectures of different block sequences and amphiphilic compositions. In section 4, we summarize our results.

2. Methods

2.1. Model

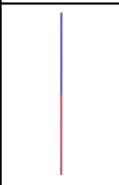
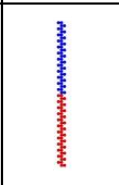
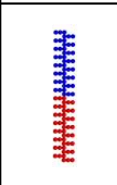
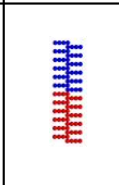
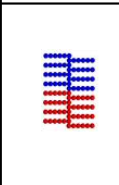
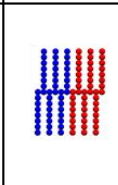
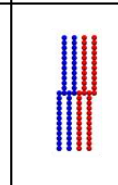
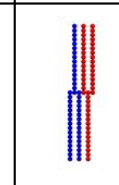
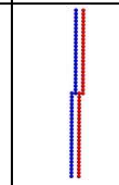
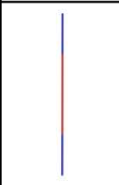
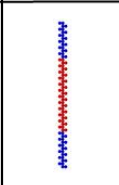

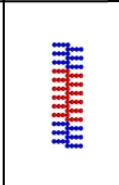
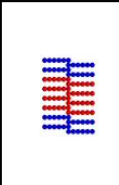
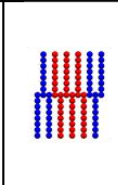
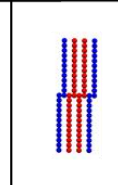
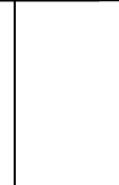
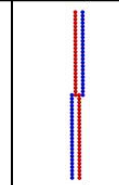
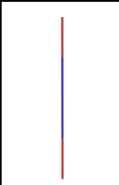
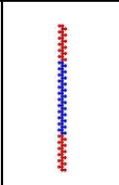
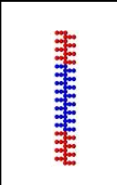
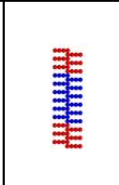
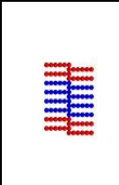
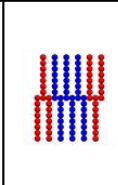
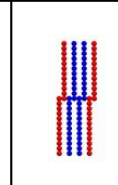
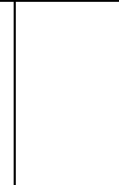
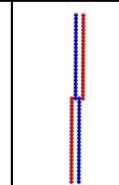
Sequence	1 $N_{bb} = 96$ $N_{sc} = 0$	2 $N_{bb} = 48$ $N_{sc} = 1$	3 $N_{bb} = 32$ $N_{sc} = 2$	4 $N_{bb} = 24$ $N_{sc} = 3$	5 $N_{bb} = 16$ $N_{sc} = 5$	6 $N_{bb} = 12$ $N_{sc} = 7$	7 $N_{bb} = 8$ $N_{sc} = 11$	8 $N_{bb} = 6$ $N_{sc} = 15$	9 $N_{bb} = 4$ $N_{sc} = 23$
AB									
ABA									
BAB									

Figure 1. Schematics of the polymer architectures with A:B 50:50 (solvophilic to solvophobic compositions) and AB, ABA and BAB block sequences. The solvophilic components are represented with blue beads (A) and the solvophobic components with red beads (B). From left to right, the backbone length (N_{bb}) decreases and the side chain length (N_{sc}) increases to maintain the same total number of beads per polymer chain ($N_{tot} = 96$). We note that for A:B 50:50, polymer architecture 8 ($N_{bb}=6$ $N_{sc}=15$) and $N_{tot}=96$ neither an ABA nor a BAB sequences are feasible. For amphiphilic compositions of A:B 75:25 and A:B 25:75 (schematics not shown in this figure) there are fewer combinations of N_{bb} and N_{sc} that provide chains with $N_{tot} = 96$.

We represent the linear and non-linear BPs, both the backbone and the side chains in the case of the branched polymer architectures, with a generic flexible coarse-grained (CG) bead-spring model.^{58,59} All the details of our CG model are similar to our recent work.⁶⁰ To be brief, we present only the key features here. All polymer beads have a diameter of $1d$, a mass $1m$, and are bonded to their neighboring beads in the chain with a harmonic spring. The equilibrium bond distance is set to $1d$ and each spring has a force

constant of $50 \varepsilon/d^2$, where all the units are in reduced Lennard-Jones units. We define N_{tot} as the total number of beads in the polymer chain, N_{bb} as the number of beads in the polymer backbone, and N_{sc} as the number of side chain beads as shown in **Figure 1**. The solvophilic components (A) are represented by blue beads and the solvophobic components (B) with red beads, where the ratio of solvophilic to solvophobic components is indicated as A:B. The solvent is modelled implicitly. The effect of the solvent quality on the solvophobic B beads is captured through a Lennard-Jones (LJ)⁶¹ interaction potential between the solvophobic B beads described as

$$U_{B-B}(r) = 4\varepsilon_{BB} \left[\left(\frac{\sigma}{r}\right)^{12} - \left(\frac{\sigma}{r}\right)^6 \right] \quad r \leq 2.5d \quad (1)$$

where σ is equal to the bead diameter ($1d$) and ε_{BB} is varied. The potential $U_{B-B}(r)$ is set to 0 for distances above the cut-off distance of $2.5d$ and the potential is shifted to have a value 0 at the cut-off distance. We use the implicit solvent representation in order to access the relevant length and time scales for block polymer assembly. Our focus is on equilibrium structure of the assembly and previous studies comparing assembly in polymer solutions with implicit and explicit solvent models have shown that the equilibrium chain conformations agree.⁶²⁻⁶⁴ To connect the above implicit solvent model, in particular the σ and ε_{BB} of **Equation 1** to specific chemistries, one could fit **Equation 1** to the potential of mean force between the center of masses of two monomers in an explicit solvent/solvent mixture calculated from atomistic simulations.⁶⁵

The assembly of amphiphilic BPs driven by the solvophobic B-B interactions, all other pair-wise non-bonded interactions between the solvophilic A beads (A-A) or the solvophilic and solvophobic beads (A-B) are modeled with the purely repulsive Weeks-Chandler-Andersen (WCA)⁶⁶ potential to capture the solvophilic nature of the A beads.

$$U_{WCA}(r) = 4\varepsilon \left[\left(\frac{\sigma}{r}\right)^{12} - \left(\frac{\sigma}{r}\right)^6 \right] + \varepsilon \quad r \leq 2^{1/6}d \quad (2)$$

where ε is 1 (in reduced LJ units); the potential $U_{WCA}(r)$ is set to 0 above the cut-off distance of $2^{1/6}d$.

We choose the above generic coarse-grained polymer model for all architectures to understand how the different connectivity in branched and linear polymer architectures impacts their assembly. To keep the model the same for all architectures, we have to maintain the backbone and side chain beads with the same size and interactions. Representing the side chains and backbones similarly is important in our study to fairly compare the bottlebrush polymer architectures with the linear and ‘star-like’ polymer architectures. This is not an unusual choice; in fact Dutta et al.⁵⁵ have shown that coarse-grained bead-spring model with all beads of equal size in bottlebrushes with one side chain per backbone bead show quantitative agreement between the intrinsic viscosity determined from experiments and simulations. In experiments, the backbone and side chain chemistries may differ drastically, and if one wishes to directly simulate a specific bottlebrush chemistry in a solvent (or solvents), they may map their model (e.g., physical sizes of the beads, interaction between the beads) to those specific chemistries and solvent mixtures. We direct the reader to discussion about such interactions to chemistry mapping given in the supplementary information of Ref.⁶⁷ and the main paper of Refs.^{68,69}.

2.2. Simulation details

Past studies have shown that there are several appropriate computational approaches to study self-assembly of amphiphilic polymers in solution (e.g., PRISM theory,^{60, 69, 70} dissipative particle dynamics (DPD),⁷¹ as well as other approaches highlighted in a recent review paper⁷²). In this paper, we use MD simulations in the canonical (NVT) ensemble using the Nosé-Hoover thermostat with the LAMMPS package.⁷³ We create the initial configuration by randomly placing 400 polymer chains with random orientations in the cubic simulation box, with the box size selected to achieve the target BP solution concentration, η , (defined as the volume of the polymer divided by the simulation volume). The simulation box volume is initially 20% larger than the desired box volume to prevent overlap between the chains in the initial configuration. We start from this larger simulation box and linearly reduce the sides of the cubic simulation box over 3,000,000 timesteps to arrive at the desired occupied volume fraction η of 0.025 at a temperature of $T^*=4$ and $\epsilon_{BB}=0.055$. Next, we set the temperature of the system to $T^*=1$ and allow the

system to equilibrate for another 3,000,000 timesteps at $\epsilon_{BB}=0.055$ to finish the equilibration stage of the simulation.

To achieve assembly of the amphiphilic BPs in solution, we perform a gradual stage-wise increase of the solvophobicity of the system (equivalent to increasing ϵ_{BB} in our procedure) which mimics experiments where the initial good solvent condition is varied by adding/exchanging with a poor solvent for the solvophobic block. We increase ϵ_{BB} by 0.009 and spend 3,000,000 timesteps at each ϵ_{BB} value. We stop this stage-wise increase of ϵ_{BB} when there is no further change in the aggregation behavior. The choice of the time spent at each stage and the increase in ϵ_{BB} between the stages is extensively tested, through both replicate simulations and more gradual changes in the solvophobicity, to ensure we produce close to equilibrium results at each ϵ_{BB} .^{89, 130} We sample independent snapshots every 300,000 timesteps; which is longer than the time required for the chain conformation autocorrelation function to decay to 0.

2.3. Analyses

We analyze the assembly morphology (*e.g.*, aggregation number, micelle size, and the packing parameter for non-spherical assemblies), assembly thermodynamics (*e.g.*, unimer to micelle transition solvophobicity and energetically favorable contacts), and chain conformations of the polymer chains during micellization.

To determine the aggregation number, we define two polymer chains as part of a micelle if their B-block center of mass is within a critical distance of a minimum number of neighbors (excluding unimers) as shown in **Figure S.1**. This critical distance is determined to include the peak of the radial distribution function of the B-block center of mass at an ϵ_{BB} above which clustering does not change with increasing ϵ_{BB} . We then use a “friends of friends” algorithm⁷⁴ to determine which chains are in which clusters. After the clusters are determined, we calculate the number of chains in each cluster i , $N_{agg,i}$ and the ensemble average aggregation number at each ϵ_{BB}

$$\langle N_{agg} \rangle = \frac{\sum_{i=1}^n N_{agg,i}}{n} \quad (3)$$

where n is the total number of micelles from the sampled configurations at that ϵ_{BB} . The radius of gyration of the micelle core for cluster i is calculated by considering only the B-beads in cluster i as indicated in

$$R_{g,core\ i}^2 = \frac{1}{N_{agg,i} N_B} \sum_{j=1}^{N_{agg,i}} \sum_k^{N_B} (\mathbf{r}_{B,jk} - \mathbf{r}_{cm\ B,i})^2 \quad (4)$$

and is then averaged over all the clusters in the system. $\mathbf{r}_{B,jk}$ is the position vector of B-bead k in chain j , N_B is the number of B beads per chain, and $\mathbf{r}_{cm\ B,i}$ is the position vector of B-bead the center of mass of the B-beads in cluster i .

We also calculate the value of ϵ_{BB} at which the system transitions from a disordered fluid-like state to ordered micelles and call it the transition solvophobicity (ϵ_{BB}^{tr}). To calculate ϵ_{BB}^{tr} , we consider the aggregation number (N_{agg}) distribution at each ϵ_{BB} and then identify ϵ_{BB}^{tr} as the point at which a distinct population of micelles start to form. As ϵ_{BB} increases, clusters start to form with $N_{agg} > 1$ and the $P(N_{agg})$ increases for $N_{agg} > 1$, until the system approaches a stable average value for N_{agg} , $\langle N_{agg} \rangle_f$. We define ϵ_{BB}^{tr} as the ϵ_{BB} at which the probability of finding clusters of $\langle N_{agg} \rangle_f$ reaches a value of 0.1. This is shown in **Figure S.2**. Recent papers^{69, 70} describe different definitions/methods to calculate ϵ_{BB}^{tr} and show that the qualitative trends remain similar regardless of the criteria used to calculate ϵ_{BB}^{tr} .

To compare the enthalpic driving forces between the different polymer architectures, we calculate the number of favorable energetic intermolecular contacts by identifying the first peak value of the B-bead intermolecular radial distribution function at a fixed solvophobicity after the chains have formed micelles that do not change with increasing solvophobicity (**Figure S.3**). This value indicates that number of beads that are within the minimum of the attractive well of the LJ potential.

We use the branching parameter⁵⁷ as a metric for defining polymer architecture. The branching parameter (g_g) is defined as the radius of gyration of the branched chain ($R_{g,b}^2$) divided by the radius of gyration of the linear chain ($R_{g,l}^2$)

$$g_g \equiv \frac{\langle R_{g,b}^2 \rangle}{\langle R_{g,l}^2 \rangle} \quad (5)$$

and is calculated at the initial solvophobicity ($\epsilon_{BB}=0.055$), where the simulation is still in a disordered fluid-like state. We choose to characterize the extent of branching in polymer architecture using the branching parameter especially since we maintain the same total number of beads in all polymer architectures. Other studies have used length of the backbone versus side chain length to characterize extent of branching going from spherical to anisotropic bottlebrushes,^{29, 30, 55, 75} and from comb to bottlebrush polymers.^{31, 32}

We also estimate the conformational entropy loss of the solvophobic (B) components upon assembly ($S_{conf, B-block}$) as follows:

$$S_{conf, B-block} = -k_B \sum_{n=1}^{states} P(R_g^2)_n \ln P(R_g^2)_n \quad (6)$$

where $P(R_g^2)_n$ is the probability that the B-block has a squared radius of gyration R_g^2 in state n and is determined for each $(R_g^2)_n$ sampled. The radius of gyration of the solvophobic (B) components is used for the calculation as the radius of gyration of the solvophilic (A) components does not change as significantly as the B-block upon assembly as seen in **Figure S.4**.

Select polymer architectures of the BAB block sequences form states where the two solvophobic blocks of one chain are split between two different micelle cores, which we will refer to as bridged conformations. The probability of different chain conformations, including bridged conformations, is indicated in **Figure S.5** for three select architectures (linear, bottle brush, and ‘star-like’) as a function of solvophobicity, ϵ_{BB} . At high ϵ_{BB} , the probability of bridging does not change with increasing ϵ_{BB} and we compare the probability of the bridged conformations at high ϵ_{BB} , $P_{bridge, f}$, between the different polymer architectures.

For the spherical and non-spherical assembly morphologies, we also calculate the packing parameter, p ,⁷⁶ as

$$p = \frac{v}{l_c A} \quad (7)$$

where V is the volume of the solvophobic block per chain in the micelle core, l_c is the length of the solvophobic block per chain within the micelle core, and A is the interfacial area between the micelle core and corona per chain, as depicted in **Figure S.6**. We calculate the packing parameter after confirming that the clusters do not change upon further increase of solvophobicity. We calculate V , the volume of the solvophobic block per chain, by

$$V = \frac{\sum_1^{N_B} V_B}{0.64} \quad (8)$$

where the numerator is the sum of the total number of solvophobic beads (N_B), each with volume V_B , for one chain and the denominator is 0.64, to account for random sphere packing and void volumes within the micelle core. To determine l_c , we use

$$l_c = \frac{1}{N_{chains} (N_B - 1)} \sum_i^{N_{chains}} \sum_j^{(N_B - 1)} \left((\mathbf{r}_{int,i} - \mathbf{r}_{ij})^2 \right)^{0.5} \quad (9)$$

which is the average distance from the B backbone bead of chain i (with the position vector $\mathbf{r}_{int,i}$) bonded to the backbone A-bead, which sits at the core-corona interface, to the rest of the B-beads (each with position vector \mathbf{r}_{ij}) within the polymer chain i , averaged over all chains (N_{chains}) in the simulation. The choice of metric for l_c is not straightforward for branched polymer architectures as each of the side chains have a different length within the micelle core. After trying various metrics to determine l_c , we find that irrespective of the choice, the qualitative trends in the packing parameter stays the same (data not shown). Finally, the interfacial area per chain, A , is determined through the solvent accessible surface area (SASA)^{77, 78} which is calculated with a solvent probe radius of $1d$. After testing different probe sizes, a probe radius of $1d$ is chosen to exclude voids in the micelle core in order to consider only the outer surface of the micellar structures. The interfacial area per chain is calculated as

$$A = \frac{SASA}{N_{chains}} \quad (10)$$

where N_{chains} is the number of polymer chains in the simulation.

2.4. Design parameters explored

To investigate the effect of different polymer architectures on the assembly of BPs, we keep the total number of beads fixed at 96 polymer beads per chain. With the fixed number of beads per chain, we are able to isolate the effect of branching while maintaining constant the energetic driving force which is simply proportional to number of solvophobic beads. To maintain the same number of beads (N_{tot}) going from linear to bottlebrush to ‘star-like’ polymers, we decrease the backbone length (N_{bb}), while simultaneously increasing the side chain length (N_{sc}). This is shown for AB, ABA, and BAB block sequences and A:B 50:50 amphiphilic composition in **Figure 1**. For example, by decreasing the backbone from $N_{bb}=96$ ($N_{sc}=0$) to $N_{bb}=24$ ($N_{sc}=3$) to $N_{bb}=4$ ($N_{sc}=23$) we vary architectures from linear to bottlebrush (long backbone with many short side chains) to ‘star-like’ (short backbone with few long side chains), respectively. Additionally, we investigate the effect of the amphiphilic BP composition and consider three cases: solvophilic-rich A:B 75:25, symmetric A:B 50:50, and solvophobic-rich A:B 25:75 for AB, ABA, and BAB BPs. All simulations are run for the occupied volume fraction of $\eta = 0.025$.

3. Results & Discussion

To describe the effect of the polymer architecture on the assembly behavior we present the micellization thermodynamics and structural characteristics in **Figure 2**. We vary polymer architectures for A:B 50:50 amphiphilic composition as indicated for the AB, ABA, and BAB BPs in **Figure 1 and 2a**. We change the polymer architectures in **Figure 1 and 2** from linear to bottlebrush to ‘star-like’, from left to right, by decreasing the backbone length (N_{bb}) and simultaneously increasing the side chain length (N_{sc}) to maintain the same total number of beads per chain ($N_{tot}=96$). Most of the micelles found for systems in **Figure 2** are spherical. We compare the solvophobicity (solvent quality) required to form micelles (ϵ_{BB}^{tr}) for each of the polymer architectures in **Figure 2b**. As we explore linear to bottlebrush architectures, ϵ_{BB}^{tr} increases indicating that a poorer solvent quality is required for bottlebrush BPs to form micelles as compared to the linear BPs. Then, from bottlebrush to ‘star-like’ architectures, ϵ_{BB}^{tr} decreases. The ABA and BAB triblock sequences exaggerate this pattern for the bottlebrush architectures and show a higher ϵ_{BB}^{tr}

than the AB diblock polymers (di-BPs) with equivalent polymer architectures. The bottlebrush tri-BPs (ABA and BAB) compared to the bottlebrush di-BPs (AB) show the largest difference in ε_{BB}^{tr} . The differences in ε_{BB}^{tr} between AB, ABA and BAB reduce as the polymer architecture become more ‘star-like’ because the ‘star-like’ BPs are similar for all three (AB, ABA, and BAB) block sequences; in these ‘star-like’ BPs, the side chains have significant conformational freedom around the short backbone (*e.g.*, for polymer architecture 9, the backbone comprised of 4 beads has four side chains that are each 23 beads long). Similarly, other structural characteristics of the ‘star-like’ BPs are also similar irrespective of the block sequence, as described next.

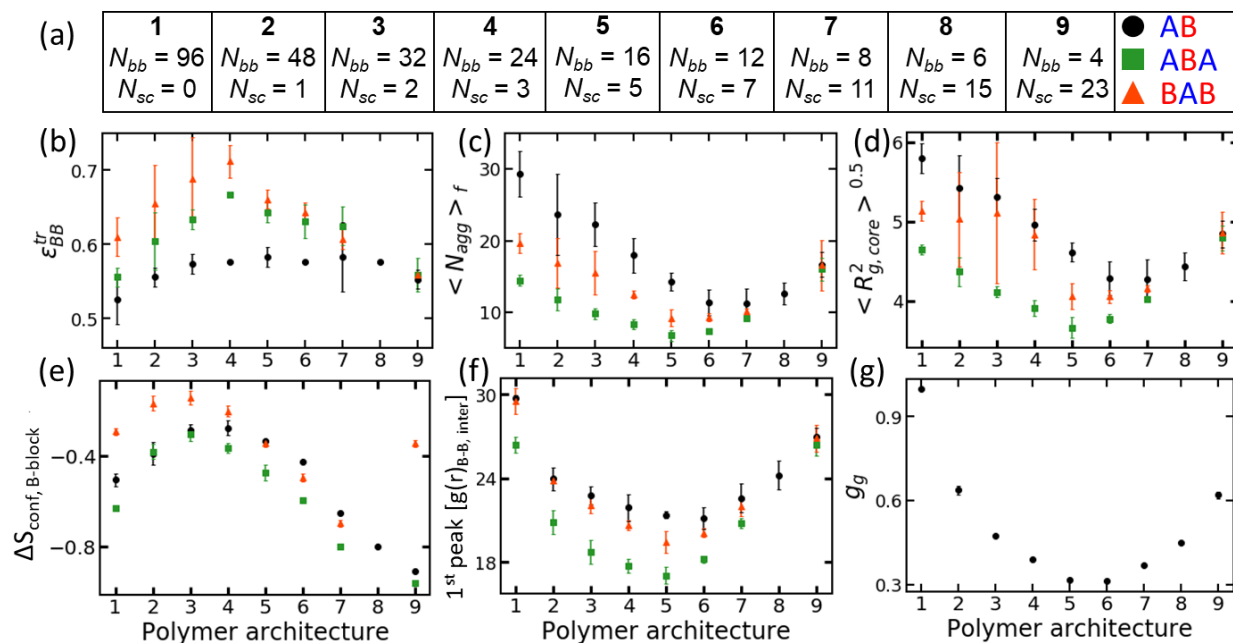


Figure 2. Micelle assembly and structural characteristics for A:B 50:50 amphiphilic BPs with AB, ABA, and BAB block sequences and (a) varying polymer architectures (also shown visually in **Figure 1**). (b) Transition solvophobicity, (c) the aggregation number at $\varepsilon_{BB}=0.91$ and (d), micelle core radius of gyration at $\varepsilon_{BB}=0.91$, (e) solvophobic block conformational entropy difference between disordered and assembled states at $\varepsilon_{BB}=0.91$, (f) first peak from the B-B intermolecular radial distribution function at $\varepsilon_{BB}=0.91$, and (g) branching parameter. The error bars indicate the 95% confidence interval between the results of three independent simulations.

The structural characteristics of the micelles formed from the different BP architectures (**Figure 2c-d**) are evaluated at $\varepsilon_{BB}=0.91$, a value of solvophobicity above which the clustering does not change with increasing ε_{BB} . For each BP sequence, as we go from linear to bottlebrush polymer architectures, both the

final aggregation number (**Figure 2c**) and the micelle core radius of gyration (**Figure 2d**) values decrease. Then, from bottlebrush to ‘star-like’ polymer architectures, the aggregation number and core radius of gyration values increase. For each of the bottlebrush polymer architectures, the ABA BPs form the smallest aggregates with the lowest aggregation number and the BAB BPs are in between. We note that we see a similar non-monotonic trend in the aggregation numbers for systems with $N_{\text{tot}}=144$ (**Figure S.7.**) and $N_{\text{tot}}=24$ (**Figure S.8.**).

Next, we evaluate how well the results presented so far agree/disagree with some past work. Published experimental results investigating the effect of block sequence have shown that for linear BPs, the tri-BPs form smaller micelles with lower aggregation numbers than di-BPs of the same molecular weight.^{8, 79, 80} Thus, the experimental results for linear BPs agree with our results for the linear BPs. Beyond the published experiments, we go on to show that for the bottlebrush polymer architectures the differences between the sequences exist, and are larger than the differences between sequences for the ‘star-like’ polymer architectures which show no discernable difference between the AB, ABA and BAB block sequences. Past experiments comparing star and linear BPs have shown that star polymer architectures have lower aggregation numbers and smaller micelle sizes than their linear equivalents,⁸ which is also captured in our simulation results shown in **Figure 2c-d**. These qualitative agreements with the experimental trends provide validation for the suitability of our generic coarse-grained model for this study.

Our results in **Figure 2c-d** show a non-monotonic pattern in the assembly characteristics as we go from linear to bottlebrush to ‘star-like’. We hypothesize that this non-monotonic behavior in the assembly characteristics stems from the topological arrangement of the solvophobic B beads and how well they are shielded/exposed in the different architectures. These topological effects should impact the thermodynamic driving forces for assembly, namely the enthalpic (*e.g.*, energetically favorable B-B contacts upon aggregation) and entropic (*e.g.*, configurational entropy loss upon assembly) contributions to the change in free energy upon BP assembly. Our initial hypothesis is that for BP systems with same number of coarse-grained A and B beads, the lengthening/shortening backbone length and increasing/decreasing number and

length of side chains should affect, primarily, the entropic contributions arising from the translational and conformational entropy of the disordered and assembled states, and that these entropic contributions would dominate the assembly behavior. We estimate the conformational entropy loss of the solvophobic B-block upon micellization as the difference between the conformational entropy of fluid-like state at low solvophobicity and that of the aggregated state at high solvophobicity. This estimate is shown for different BP architectures in **Figure 2e**. The trends in conformational entropy loss upon assembly for varying BP architecture is the *opposite* of what would be required to explain the assembly behavior in **Figures 2b-c**. One would expect that a BP architecture with higher ϵ_{BB}^{fr} requires stronger enthalpic interactions to aggregate and compensate for a larger loss in conformational entropy upon aggregation. This means that as bottlebrush architectures have a higher ϵ_{BB}^{fr} , they should have larger loss in conformational entropy upon aggregation. Instead, the conformational entropy loss upon aggregation is lower for the bottlebrush polymer architectures than for the linear or the ‘star-like’ polymer architectures. The bottlebrush chains are compact (*i.e.*, few possibilities of conformations) with dense local packing of the side chains along the polymer backbone and thus, do not lose as many conformations upon assembly. The ‘star-like’ polymer architecture loses the most conformational entropy upon assembly because the long solvophobic and solvophilic side chains on short backbones easily interchange positions and fluctuate around the short backbone in favorable solvent conditions. Upon micellization, this conformational freedom of solvophobic and solvophilic side chains in the ‘star-like’ polymer is curtailed as the solvophobic and solvophilic side chains separate to the core and corona, respectively, resulting in a big loss in adoptable conformations. We note that for the BAB sequences, the conformational entropy loss is calculated separately for each of the B-blocks. As such, the conformational entropy loss for the BAB polymer architecture 9 ($N_{bb}=4$ $N_{sc}=23$) in **Figure 2e** shows a different behavior than would be expected, compared to the behavior in the AB and ABA block sequences, because each of the solvophobic ends for polymer architecture 9 are linear.

Next, we consider the other thermodynamic driving force for assembly, namely the enthalpic gain upon assembly (due to the aggregation of the solvophobic (B) beads) for the different BP architectures. In

Figure 2f, we compare the number of favorable energetic contacts for the various BP architectures by considering the height of the first peak in the inter-molecular B bead radial distribution function for the different BP architectures after stable aggregates have formed ($\epsilon_{BB}=0.91$). This describes the number of nearest B bead neighbors that each B bead has; the higher the value of the first peak the higher the number of neighbors. The behavior of the number of nearest neighbor contacts in **Figure 2f** explains the behavior in **Figures 2b-c**. The system that has fewer nearest neighbors upon assembly also needs a higher solvophobicity to transition, ϵ_{BB}^{tr} . This conclusion remains unchanged even if we calculate the number of intermolecular B-B contacts only within the interior of the micelle core (**Figure S.10.**) and avoid the effect of micelle sizes (and surface areas) that one may think impacts the results in **Figure 2f**. This means that the solvophobicity needed for assembly of polymers with varying architecture at constant molecular weight is dominated by how shielded/exposed the solvophobic beads are to make those energetically favorable solvophobic contacts. The total entropic contributions also have an important role in the assembly, for example: while the intermolecular contacts are less for the bottlebrush ABA BPs than the bottlebrush BAB BPs, the ϵ_{BB}^{tr} is larger for the bottlebrush BAB BPs than the ABA BPs.

To establish a general metric of comparison between the various branched polymer architectures and linear polymer architectures of the same molecular weight, in **Figure 2g**, we characterize the polymer architectures by their branching parameter.^{57, 81} The branching parameter is calculated at low solvophobicity ($\epsilon_{BB}=0.045$) when the system is in a disordered fluid-like state and the chains are in their unimer state, by dividing the radius of gyration of the branched polymer architecture by the radius of gyration of the linear polymer architecture. The behavior of the branching parameter, g_g , with changing polymer architecture (**Figure 2g**) follows a similar trend to the aggregation number (**Figure 2c**), indicating that this is could be a useful metric for designing and predicting the assembly behavior of the branched polymers from the radius of gyration of the chains before assembly.

Using this branching parameter, g_g , as a metric to describe the polymer architectures, we plot the transition solvophobicity (ϵ_{BB}^{tr}), the final aggregation number, and the micelle core radius of gyration as a function of g_g in **Figure 3**. For AB di-BPs, the ϵ_{BB}^{tr} decreases monotonically in **Figure 3b** with increasing g_g . For the ABA and BAB tri-BPs, however, the results in **Figures 3b, 3c and 3d** show that in addition to g_g , the classification of branching (*i.e.*, chains with $N_{bb} > N_{sc}$ or chains with $N_{bb} < N_{sc}$) affects the ϵ_{BB}^{tr} . At a similar g_g , polymer architectures with $N_{bb} > N_{sc}$, which we broadly classify as bottlebrush, have a higher ϵ_{BB}^{tr} than the ‘star-like’ polymer architectures with $N_{bb} < N_{sc}$. As mentioned before, the assembly and structural characteristics of the ‘star-like’ polymer architecture for block sequences AB, ABA, and BAB are all within error of each other.

For the di-BPs in **Figures 3e and 3h**, the aggregation number and the micelle core radius of gyration behave similarly, with both being higher for the bottlebrush polymer architectures ($N_{bb} > N_{sc}$) than the ‘star-like’ polymer architectures ($N_{bb} < N_{sc}$). Going from AB to ABA to BAB block sequences, both the aggregation number (**Figure 3e-g**) and the micelle core radius of gyration (**Figure 3h-j**) reduce for the bottlebrush architectures, resulting in a more monotonic change of these characteristics as a function of the branching parameter, g_g .

So far, the results we presented are BPs with A:B 50:50, symmetric BP composition. We also calculate the micellization thermodynamics and structural behaviors for: A:B 75:25 (*solvophilic*-rich) and 25:75 (*solvophobic*-rich) in **Figures 4 and 5**, respectively. A similar comparison with regards to the branching parameter could be done for these amphiphilic compositions, but for the sake of brevity and clarity in the comparison between the different polymer architectures and block sequences, we show the results versus polymer architecture number as done in **Figure 2**.

Both A:B 75:25 (**Figure 4b**) and 25:75 (**Figure 5b**) show a non-monotonic behavior similar to the A:B 50:50 (**Figure 2b**) polymers for ϵ_{BB}^{tr} with changing polymer architecture, suggesting that for the cases studied, at the same total number of beads, the polymer architecture affects assembly thermodynamics in a

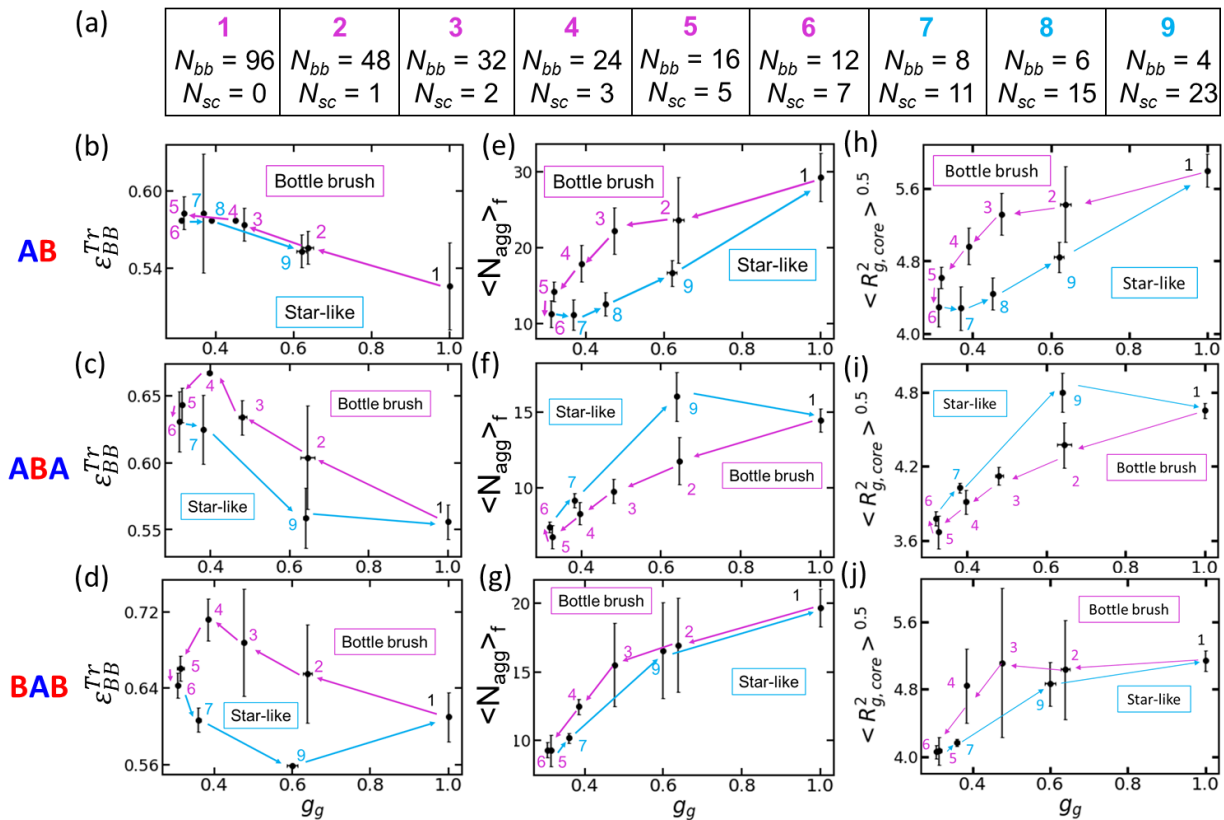


Figure 3. Micelle assembly and structural characteristics for various (a) polymer architectures as a function of the branching parameter for polymers of A:B 50:50 amphiphilic composition and AB, ABA, and BAB block sequences. Transition solvophobicity (b-d), the aggregation number at $\epsilon_{BB}=0.91$ (e-g), and the micelle core radius of gyration at $\epsilon_{BB}=0.91$ (h-j). The error bars indicate the 95% confidence interval between the results of three independent simulations.

similar way regardless of amphiphilic composition or block sequence. Following the behavior established for linear polymers through past experiments and simulations, increasing the solvophobic composition reduces the CMC (similar to reducing the ϵ_{BB}^{Tr} at fixed concentration) because BPs with larger number of solvophobic B beads need smaller solvophobicity (enthalpic driving force) to induce assembly. In contrast to A:B 50:50 and A:B 75:25 (**Figures 2 and 4**), the BAB BPs with A:B 25:75 (**Figure 5**) show a lower ϵ_{BB}^{Tr} than the AB and ABA block sequences. We hypothesize that the majority solvophobic component in the BAB sequence shields the repulsion of the solvophilic A block at the center of the BAB BPs, reducing the ϵ_{BB}^{Tr} more than the AB and ABA sequences.

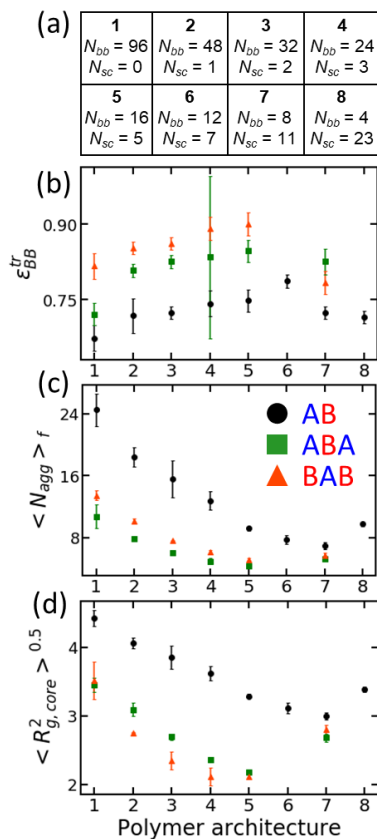


Figure 4. Micelle assembly and structural characteristics for (a) different polymer architectures with A:B 75:25 amphiphilic composition (solvophilic-rich) and AB, ABA, and BAB block sequences. (b) Transition solvophobicity, (c) the aggregation number at $\varepsilon_{BB}=1.00$, and (d) micelle core radius of gyration at $\varepsilon_{BB}=1.00$. The error bars indicate the 95% confidence interval between the results of three independent simulations.

The structural behavior of the solvophilic-rich composition A:B 75:25 in **Figure 4c-d** shows a similar behavior to the A:B 50:50 BPs, although the values are smaller than those in **Figure 2c**, and like A:B 50:50 all of the assemblies here are spherical. Interestingly, for all polymer architectures of ABA and BAB block sequences, the differences between the ε_{BB}^{tr} , the aggregation number, and the micelle core radius of gyration reduce, resulting in a similar assembly behavior for the ABA and BAB block sequences.

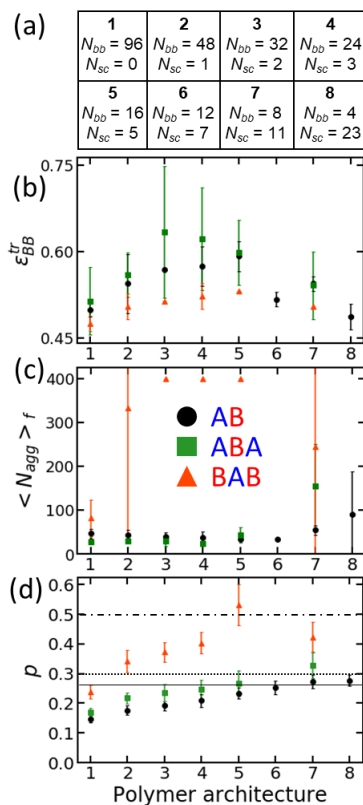


Figure 5. (a) – (c) Same as Figure 4 but for A:B 25:75 amphiphilic composition. (d) Chain packing parameter, p with horizontal lines as guides for critical values of the packing parameter. The micelle structural characteristics in this figure are calculated at $\epsilon_{BB}=0.63$.

The solvophobic-rich BP system (A:B 25:75) discussed in **Figures 5**, show different assembly morphologies depending on the polymer architecture and the block sequence. The large aggregation numbers in **Figure 5c** for the BAB block sequences are due to all of the chains in the simulation box aggregating to form a single cluster, visualized in **Figure 6**. The packing of the chains and the resulting assembly is quantified by the chain packing parameter,⁷⁶ p , for each system after the micelles have formed (**Figure 5d**). Representative simulation box visualization of the resulting assemblies is presented in **Figure 6**. From the well-established trends in the packing parameter,⁷⁶ values below 0.33 (the dotted line in **Figure 5d**) indicate spherical morphologies, values between 0.33 and 0.5 (the dashed-dotted line in **Figure 5d**) indicate cylindrical morphologies, and values between 0.5 and 1 indicate vesicle morphologies. We caution the reader that this analysis from simulations is sensitive to the criteria used to calculate the chain length within the micelle structure (**Equations 7 and 9**), despite this we see that the trend in the behavior of the

calculated packing parameters remains consistent regardless of the exact criteria used. There are also additional sources of error introduced by the selection of the probe size to determine the solvent accessible surface area (SASA) (**Equation 10**) and with the approximation to determine the aggregate volume (**Equation 8**) as these implicit solvent simulations do not account for any potential swelling of the core through the uptake of solvent. As such we propose the solid horizontal line in **Figure 5d** as a shift of the dotted line to indicate the change between spherical and cylindrical assembly morphologies to account for the potential sources of error in our calculations. Despite all of the sources of uncertainty, the agreement in the change of packing parameter values and the resulting micelle morphology is good, with the increase in the packing parameter coinciding with the micelle morphology transition from spherical to cylindrical to bilayer micelle structures.

For the AB di-BPs (A:B 25:75), going from linear to bottlebrush polymer architectures, all of the micelle morphologies are spherical in **Figure 6**. In contrast, the ‘star-like’ polymer architectures starting from polymer architecture 7 ($N_{bb}=8$ and $N_{sc}=11$) form cylindrical micelle morphologies. Similarly, there is an increase in the packing parameter in **Figure 5d**, as the polymer architecture goes from linear to bottlebrush to ‘star-like’, indicating a monotonic flattening of the core-corona interface as the packing parameter increases, and the micelle morphologies changes from spherical to cylindrical after a critical value (suggested by the solid horizontal line) is reached. Going from AB to ABA or BAB there is an increased tendency to flatten the core-corona interface; correspondingly the ABA and BAB sequences have higher packing parameter values than the AB BPs in **Figure 5d**. The ABA tri-BPs show a monotonic increase in the packing parameter similar to the AB di-BPs, although the ABA micelle morphology is cylindrical for most branched polymer architectures as compared to AB di-BPs. Correspondingly, all the packing parameter values are shifted to higher values for the ABA sequence as compared to AB sequence. For the BAB BPs in **Figure 5d**, going from linear to bottlebrush, the packing parameter increases significantly and micelle morphology changes from spherical to cylindrical and to bilayer in **Figure 6**. Thus, for solvophobic-rich systems, the assembly morphology and curvature of the core-corona interface

are a stronger function of polymer architecture and block sequence than for solvophilic-rich or symmetric BPs.

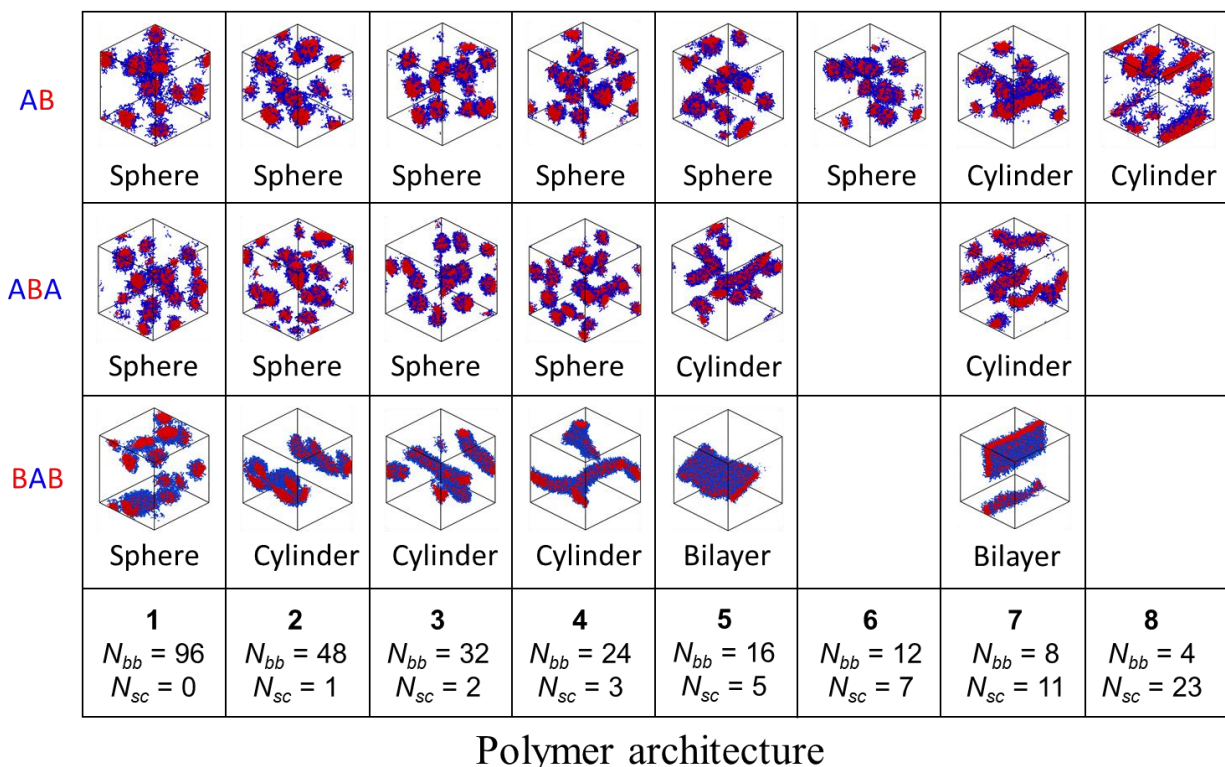


Figure 6. Representative simulation snapshots of assembled morphologies for varying polymer architectures with A:B 25:75 amphiphilic composition (solvophobic-rich) and AB, ABA, and BAB block sequences at $\epsilon_{BB}=0.63$. The simulation images are shown at $\epsilon_{BB}=0.63$ which is the value of solvophobicity after the number of chains per cluster reach a plateau value and do not change further with increasing solvophobicity. We note that for an amphiphilic composition of A:B 25:75 neither ABA nor BAB polymer architectures 6 ($N_{bb}=12$ $N_{sc}=7$) and 8 ($N_{bb}=4$ $N_{sc}=23$) are feasible with $N_{tot}=96$.

One feature that is unique to the BAB sequences, is the ‘bridging’ chain conformation. In this conformation, chains form ‘bridges’ between two micelle cores under certain conditions where a chain has each of its two solvophobic blocks in two different micelle cores as visualized in **Figure 7b**. As bridging of micelles can drive gel formation and impact the resulting materials rheological properties, we quantify the impact of the polymer architecture on the propensity for bridging. The plateau probability of the chains

to bridge two micelle cores defined as the probability of the chains to bridge two micelle cores after clustering stops to change with increasing solvophobicity (which occurs at different solvophobicities for the different amphiphilic compositions) is shown in **Figure 7c**. Regardless of the amphiphilic composition, going from linear to bottlebrush polymer architectures, the probability for bridging reduces significantly until no chains form bridges for the ‘star-like’ polymer architectures. As the backbone length decreases from linear to bottlebrush polymer architecture, it becomes more favorable for the chain ends to loop back into the same micelle core (as indicated by the reduced probability of bridging) in order to avoid the larger energetic penalty of bringing two micelle cores (and their accompanying coronas) closer together. This explanation is also applicable to the behavior of the different amphiphilic compositions, where despite the reduced enthalpic driving for the A:B 75:25 BPs to form bridges (as there are fewer B-beads per solvophobic block), the increased distance between the solvophobic blocks (as solvophobic beads are replaced by solvophilic beads to achieve the relevant amphiphilic ratio) favors bridging as the micelle cores are formed further apart. Lastly, we also show that the extent of bridging is sensitive to the polymer concentration (**Figure S.11**), but the qualitative trend of propensity for bridging with varying polymer architecture remains similar. The propensity for bridging is increased with increasing polymer concentration as the entropic penalties for bridging conformations reduce due to polymer crowding.

4. Conclusions

The polymer architecture is known to affect micellar characteristics and non-linear polymer architectures are now being synthesized and used to assemble micelles with specific features, such as micelle structure, aggregation number, and unimer to micelle transition, that are different from those formed using linear polymer architectures. In this computational paper we show results that serve as guidelines for predicting micellar assembly as a function of polymer architecture, sequence and composition in varying solvent conditions. As we go from linear to bottlebrush to ‘star-like’ polymer architectures (maintaining the same molecular weight) we find a non-monotonic change in the transition solvophobicity, aggregation number,

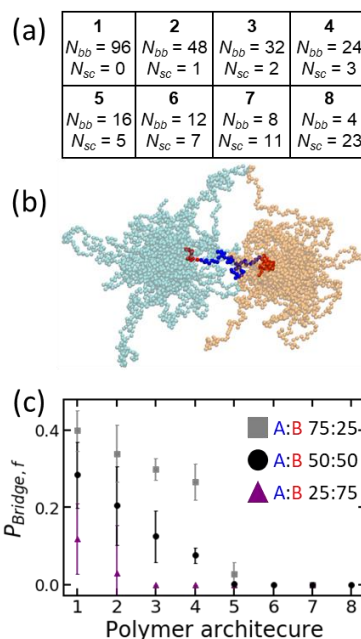


Figure 7. Polymer bridging characteristics for (a) varying polymer architectures with BAB block sequence. (b) Sample snapshot highlighting a chain bridging between two micelles of different color. (c) Final (plateau) probability for a chain to bridge two micelles of A:B 75:25, 50:50, and 25:75 composition. The values are calculated at $\epsilon_{BB}=0.63, 0.91,$ and 1.00 for A:B 75:25, 50:50, and 25:75, respectively. The error bars indicate the 95% confidence interval between the results of three independent simulations.

and core micelle size. For the bottlebrush polymer architectures, the aggregation number and micelle size decreases and the transition solvophobicity increases (*i.e.*, requires more poor solvent to form micelles) as compared to linear and ‘star-like’ architectures. The non-monotonic behavior is driven by the reduced favorable intermolecular contacts for the branched polymer architectures (with many short branches) compared to linear polymer architectures or ‘star-like’ architecture (with few long branches). Additionally, the block sequence and amphiphilic composition change the effect of the different polymer architectures (linear, bottlebrush and ‘star-like’) on micelle assembly. We are able to find some universal trends as a function of the branching parameter (the radius of the gyration of the branched chain divided by the linear chain in unimer state). We find that the ‘star-like’ polymer architecture (few long branches) exhibits similar assembly thermodynamics and structure regardless of the block sequence. The polymer architecture also influences the core-corona interface, flattening the core-corona curvature for solvophobic-rich polymers,

as the polymer architecture goes from linear to bottlebrush to ‘star-like’.

Overall, these results indicate general design strategies based on the radius of gyration of the polymer chains for a range of polymer architectures, amphiphilic compositions, and block sequences. These trends can be used to target specific micelle characteristics, such as the micelle structure and stability in solution, in order to tune the micelle for a specific application.

Conflicts of interest

There are no conflicts of interest to declare.

Acknowledgments

We acknowledge financial support from the National Science Foundation under grant number NSF DMREF-1629156. We thank K. Wooley, D. Pochan, W. Johnson and their research groups for valuable feedback during the course of this work. This research was supported in part through the use of Information Technologies (IT) resources at the University of Delaware, specifically the high-performance computing resources of the Farber supercomputing cluster, and the Extreme Science and Engineering Discovery Environment (XSEDE) Stampede cluster at the University of Texas.

References

1. L. I. Atanase and G. Riess, *Polymers*, 2018, **10**, 62.
2. A. Blanz, S. P. Armes and A. J. Ryan, *Macromol. Rapid Commun.*, 2009, **30**, 267-277.
3. N. S. Cameron, M. K. Corbierre and A. Eisenberg, *Canadian journal of chemistry*, 1999, **77**, 1311-1326.
4. H. K. Cho, I. W. Cheong, J. M. Lee and J. H. Kim, *Korean J. Chem. Eng.*, 2010, **27**, 731-740.
5. K. Kataoka, A. Harada and Y. Nagasaki, *Advanced drug delivery reviews*, 2001, **47**, 113-131.
6. K. Letchford and H. Burt, *Eur. J. Pharm. Biopharm.*, 2007, **65**, 259 - 269.
7. R. K. O'Reilly, C. J. Hawker and K. L. Wooley, *Chem. Soc. Rev.*, 2006, **35**, 1068-1083.
8. G. Riess, *Prog. Polym. Sci.*, 2003, **28**, 1107-1170.
9. J. Rodriguez-Hernandez, F. Chécot, Y. Gnanou and S. Lecommandoux, *Progress in Polymer Science*, 2005, **30**, 691-724.
10. A. Rösler, G. W. M. Vandermeulen and H.-A. Klok, *Advanced drug delivery reviews*, 2012, **64**, 270-279.
11. R. Verduzco, X. Li, S. L. Pesek and G. E. Stein, *Chem. Soc. Rev.*, 2015, **44**, 2405-2420.
12. C. Wang, Z. Wang and X. Zhang, *Accounts of chemical research*, 2012, **45**, 608-618.
13. G. Xie, M. R. Martinez, M. Olszewski, S. S. Sheiko and K. Matyjaszewski, *Biomacromolecules*, 2018, **20**, 27-54.
14. F. S. Bates, *Science*, 1991, **251**, 898-905.
15. F. S. Bates and G. H. Fredrickson, *Annu. Rev. Phys. Chem.*, 1990, **41**, 525-557.
16. Y. Mai and A. Eisenberg, *Chem. Soc. Rev.*, 2012, **41**, 5969-5985.
17. T. Smart, H. Lomas, M. Massignani, M. V. Flores-Merino, L. R. Perez and G. Battaglia, *Nano Today*, 2008, **3**, 38-46.
18. E. B. Zhulina, M. Adam, I. LaRue, S. S. Sheiko and M. Rubinstein, *Macromolecules*, 2005, **38**, 5330-5351.

19. U. Tritschler, S. Pearce, J. Gwyther, G. R. Whittell and I. Manners, *Macromolecules*, 2017, **50**, 3439-3463.
20. E. B. Zhulina and O. V. Borisov, *Macromolecules*, 2012, **45**, 4429-4440.
21. C. L. McCormick, B. S. Sumerlin, B. S. Lokitz and J. E. Stempka, *Soft Matter*, 2008, **4**, 1760-1773.
22. B. Zhang, F. Gröhn, J. S. Pedersen, K. Fischer and M. Schmidt, *Macromolecules*, 2006, **39**, 8440-8450.
23. S. Rathgeber, T. Pakula, A. Wilk, K. Matyjaszewski and K. L. Beers, *J. Chem. Phys.*, 2005, **122**, 124904.
24. S. Rathgeber, T. Pakula, A. Wilk, K. Matyjaszewski, H. il Lee and K. L. Beers, *Polymer*, 2006, **47**, 7318-7327.
25. S. S. Sheiko, B. S. Sumerlin and K. Matyjaszewski, *Prog. Polym. Sci.*, 2008, **33**, 759-785.
26. M. Zhang and A. H. E. Müller, *J. Polym. Sci., Part A: Polym. Chem.*, 2005, **43**, 3461-3481.
27. W. F. Daniel, J. Burdyńska, M. Vatankhah-Varnoosfaderani, K. Matyjaszewski, J. Paturej, M. Rubinstein, A. V. Dobrynin and S. S. Sheiko, *Nature materials*, 2016, **15**, 183.
28. S. S. Sheiko, J. Zhou, J. Arnold, D. Neugebauer, K. Matyjaszewski, C. Tsitsilianis, V. V. Tsukruk, J.-M. Y. Carrillo, A. V. Dobrynin and M. Rubinstein, *Nature materials*, 2013, **12**, 735.
29. A. Chremos and J. F. Douglas, *The Journal of Chemical Physics*, 2018, **149**, 044904.
30. A. E. Levi, J. Lequeieu, J. D. Horne, M. W. Bates, J. M. Ren, K. T. Delaney, G. H. Fredrickson and C. M. Bates, *Macromolecules*, 2019, **52**, 1794-1802.
31. H. Liang, Z. Cao, Z. Wang, S. S. Sheiko and A. V. Dobrynin, *Macromolecules*, 2017, **50**, 3430-3437.
32. J. Paturej, S. S. Sheiko, S. Panyukov and M. Rubinstein, *Science advances*, 2016, **2**, e1601478.
33. J. Bolton, T. S. Bailey and J. Rzayev, *Nano letters*, 2011, **11**, 998-1001.
34. A. Chremos and P. E. Theodorakis, *Acs Macro Letters*, 2014, **3**, 1096-1100.
35. Y. Gai, D.-P. Song, B. M. Yavitt and J. J. Watkins, *Macromolecules*, 2017, **50**, 1503-1511.
36. R. Fenyves, M. Schmutz, I. J. Horner, F. V. Bright and J. Rzayev, *J. Am. Chem. Soc.*, 2014, **136**, 7762-7770.

37. Z. Li, J. Ma, C. Cheng, K. Zhang and K. L. Wooley, *Macromolecules*, 2010, **43**, 1182-1184.
38. Z. Li, J. Ma, N. S. Lee and K. L. Wooley, *J. Am. Chem. Soc.*, 2011, **133**, 1228-1231.
39. Y. Shi, W. Zhu, D. Yao, M. Long, B. Peng, K. Zhang and Y. Chen, *ACS Macro Letters*, 2013, **3**, 70-73.
40. H. Unsal, S. Onbulak, F. Calik, M. Er-Rafik, M. Schmutz, A. Sanyal and J. Rzayev, *Macromolecules*, 2017, **50**, 1342-1352.
41. P. Xu, H. Tang, S. Li, J. Ren, E. Van Kirk, W. J. Murdoch, M. Radosz and Y. Shen, *Biomacromolecules*, 2004, **5**, 1736-1744.
42. X. Lian, D. Wu, X. Song and H. Zhao, *Macromolecules*, 2010, **43**, 7434-7445.
43. C. Luo, C. Chen and Z. Li, *Pure and Applied Chemistry*, 2012, **84**, 2569-2578.
44. H.-i. Lee, K. Matyjaszewski, S. Yu-Su and S. S. Sheiko, *Macromolecules*, 2008, **41**, 6073-6080.
45. M. Alaboalirat, L. Qi, K. J. Arrington, S. Qian, J. K. Keum, H. Mei, K. C. Littrell, B. G. Sumpter, J.-M. Y. Carrillo and R. Verduzco, *Macromolecules*, 2018, **52**, 465-476.
46. H.-P. Hsu, W. Paul and K. Binder, *EPL (Europhysics Letters)*, 2006, **76**, 526.
47. H.-P. Hsu, W. Paul and K. Binder, *Macromol. Theory Simul.*, 2007, **16**, 660-689.
48. H.-Y. Chang, Y.-L. Lin, Y.-J. Sheng and H.-K. Tsao, *Macromolecules*, 2012, **45**, 4778-4789.
49. N. G. Fytas and P. E. Theodorakis, *Materials Research Express*, 2014, **1**, 015301.
50. P. E. Theodorakis, W. Paul and K. Binder, *The European Physical Journal E*, 2011, **34**, 52.
51. P. E. Theodorakis, W. Paul and K. Binder, *Macromolecules*, 2010, **43**, 5137-5148.
52. J. Wang, K. Guo, L. An, M. Müller and Z.-G. Wang, *Macromolecules*, 2010, **43**, 2037-2041.
53. A. Polotsky, M. Charlaganov, Y. Xu, F. A. M. Leermakers, M. Daoud, A. H. E. Müller, T. Dotera and O. Borisov, *Macromolecules*, 2008, **41**, 4020-4028.
54. Z. Wang, X. Wang, Y. Ji, X. Qiang, L. He and S. Li, *Polymer*, 2018, **140**, 304-314.
55. S. Dutta, M. A. Wade, D. J. Walsh, D. Guironnet, S. A. Rogers and C. E. Sing, *Soft Matter*, 2019, **Advance Article**, 10.1039.

56. E. B. Zhulina and O. V. Borisov, *ACS Macro Letters*, 2013, **2**, 292-295.
57. J. F. Douglas, J. Roovers and K. F. Freed, *Macromolecules*, 1990, **23**, 4168-4180.
58. D. Ceperley, M. H. Kalos and J. L. Lebowitz, *Phys. Rev. Lett.*, 1978, **41**, 313-316.
59. G. S. Grest and K. Kremer, *Phys. Rev. A*, 1986, **33**, 3628-3631.
60. I. Lyubimov, M. G. Wessels and A. Jayaraman, *Macromolecules*, 2018, **51**, 7586-7599.
61. J. E. Jones, *Proc R Soc Lond A Math Phys Sci*, 1924, **106**, 441-462.
62. G. Reddy and A. Yethiraj, *Macromolecules*, 2006, **39**, 8536-8542.
63. J. R. Spaeth, I. G. Kevrekidis and A. Z. Panagiotopoulos, *J. Chem. Phys.*, 2011, **135**, 184903.
64. S. Wang and R. G. Larson, *Macromolecules*, 2015, **48**, 7709-7718.
65. T. E. Gartner III and A. Jayaraman, *Macromolecules*, 2019, **52**, 755-786.
66. J. D. Weeks, D. Chandler and H. C. Andersen, *J. Chem. Phys.*, 1971, **54**, 5237-5247.
67. Z. Zhang, J.-M. Y. Carrillo, S.-k. Ahn, B. Wu, K. Hong, G. S. Smith and C. Do, *Macromolecules*, 2014, **47**, 5808-5814.
68. D. J. Beltran-Villegas and A. Jayaraman, *Journal of Chemical & Engineering Data*, 2018, **63**, 2351-2367.
69. D. J. Beltran-Villegas, I. Lyubimov and A. Jayaraman, *Molecular Systems Design & Engineering*, 2018, **3**, 453-472.
70. I. Lyubimov, D. J. Beltran-Villegas and A. Jayaraman, *Macromolecules*, 2017, **50**, 7419-7431.
71. M. A. Johnston, W. C. Swope, K. E. Jordan, P. B. Warren, M. G. Noro, D. J. Bray and R. L. Anderson, *The Journal of Physical Chemistry B*, 2016, **120**, 6337-6351.
72. Q. Zhang, J. Lin, L. Wang and Z. Xu, *Progress in Polymer Science*, 2017, **75**, 1-30.
73. S. Plimpton, *Journal of Computational Physics*, 1995, **117**, 1-19.
74. M. E. J. Newman and R. M. Ziff, *Phys. Rev. E*, 2001, **64**, 016706.
75. S. L. Pesek, X. Li, B. Hammouda, K. Hong and R. Verduzco, *Macromolecules*, 2013, **46**, 6998-7005.
76. J. N. Israelachvili, D. J. Mitchell and B. W. Ninham, *J. Chem. Soc. Faraday Trans.*, 1976, **72**, 1525-1568.

77. B. Lee and F. M. Richards, *Journal of molecular biology*, 1971, **55**, 379-400.
78. A. Shrake and J. A. Rupley, *Journal of molecular biology*, 1973, **79**, 351-371.
79. H. Altinok, G.-E. Yu, S. K. Nixon, P. A. Gorry, D. Attwood and C. Booth, *Langmuir*, 1997, **13**, 5837-5848.
80. C. Booth and D. Attwood, *Macromolecular Rapid Communications*, 2000, **21**, 501-527.
81. B. H. Zimm and W. H. Stockmayer, *J. Chem. Phys.*, 1949, **17**, 1301-1314.

for **Table of Contents** use only

